

# Preparation and Characterization of Cu-doped TiO<sub>2</sub> nanomaterials with Anatase/rutile/brookite Triphasic Structure and their Photocatalytic Activity

**Xiaodong Zhu**

Chengdu University

**Qin Zhou**

Chengdu University

**Yangwen Xia**

Chengdu University

**Juan Wang**

Chengdu University

**Hongjin Chen**

Chengdu University

**Qiao Xu**

Chengdu University

**Jiawei Liu**

Chengdu University

**Wei Feng** (✉ [fengwei233@126.com](mailto:fengwei233@126.com))

Chengdu University <https://orcid.org/0000-0002-4318-8520>

**Shanhua Chen**

Chengdu University of Technology

---

## Research Article

**Keywords:** Cu-TiO<sub>2</sub>, triphasic structure, photocatalytic activity, rhodamine B

**Posted Date:** June 14th, 2021

**DOI:** <https://doi.org/10.21203/rs.3.rs-262894/v1>

**License:**  This work is licensed under a Creative Commons Attribution 4.0 International License.

[Read Full License](#)

---

**Version of Record:** A version of this preprint was published at Journal of Materials Science: Materials in Electronics on July 26th, 2021. See the published version at <https://doi.org/10.1007/s10854-021-06660>

5.

# Abstract

Pure TiO<sub>2</sub> and different concentrations of Cu-doped TiO<sub>2</sub> with anatase/rutile/brookite triphasic structure were successfully synthesized through a simple hydrothermal process and characterized by X-ray diffraction (XRD), Raman, scanning electron microscope (SEM), transmission electron microscope (TEM), X-ray photoelectron spectra (XPS), diffuse reflectance spectra (DRS), photoluminescence spectra (PL) and Brunauer-Emmett-Teller surface area (BET). Both pure and Cu-doped TiO<sub>2</sub> show relatively high photocatalytic activity owing to their considerable surface areas. Moreover, the three-phase coexisting structure and the conversion between Cu<sup>2+</sup> and Cu<sup>+</sup> ions facilitate the separation of photogenerated electrons and holes, which is favorable for photocatalytic performance. 1%Cu-TiO<sub>2</sub> exhibits the highest photocatalytic activity and the degradation degree of rhodamine B (RhB) reaches 93.5% after 30 min, which is higher than that of monophasic/biphasic 1%Cu-TiO<sub>2</sub>. ·O<sub>2</sub><sup>-</sup> radical is the main active specie, and h<sup>+</sup> and ·OH are subsidiary in the degradation process.

## 1 Introduction

Degradation of water pollutants by photocatalysts is a promising technology because of its environmental protection and validity [1–3]. Several candidate photocatalysts have been used in water treatment such as ZnO [4, 5], SrTiO<sub>3</sub> [6], CdS [7] and so on. Among many different photocatalysts, TiO<sub>2</sub> materials are extensively investigated due to its high chemical stability, high efficiency, availability and nontoxicity [8–12]. However, TiO<sub>2</sub> absorbs only ultraviolet light which is less than 5% of sunlight. Besides, the high recombination rate of photoinduced charge carriers is another drawback [1, 2]. It is necessary to modify it and metal ions doping is a simple and effective modification way. It has been widely reported that Cu doping can modify the structure of TiO<sub>2</sub> and enhance the photocatalytic activity [13, 14].

There are three crystal phases of TiO<sub>2</sub>: anatase, rutile and brookite. Anatase TiO<sub>2</sub> or rutile TiO<sub>2</sub> has been synthesized by various methods and their photocatalytic performance is widely studied. In addition, a lot of researches focus on preparing mixed phase TiO<sub>2</sub> with excellent photocatalytic activity. The reason for the higher photocatalytic activity of mixed phase TiO<sub>2</sub> than single-phase TiO<sub>2</sub> is that the conduction band positions of the three phases are different. Therefore, photogenerated electrons can move from the phase with higher conduction band to the phase with lower conduction band, inhibiting the recombination of photogenerated electrons and holes and improving the quantum efficiency [12, 15]. For instance, Li et al. [15] successfully synthesized TiO<sub>2</sub> photocatalysts with different proportions of anatase and rutile mixed phases in an acidic hydrothermal system. The photodegradation of rhodamine B (RhB) and methyl orange (MO) results show that the mixed phase TiO<sub>2</sub> samples display better photocatalytic performance, and the catalyst containing 77 wt. % anatase and 23 wt. % rutile exhibits the highest photocatalytic activity. Cao et al. [16] prepared brookite TiO<sub>2</sub> with different rutile contents by a facile solvothermal method. TiO<sub>2</sub> consisted of 28 wt. % rutile and 72 wt.% brookite exhibits the highest degradation rate. The researches on TiO<sub>2</sub> with anatase/rutile/brookite triphasic structure have also been

reported [10, 17]. Based on two-phase mixed  $\text{TiO}_2$ , since the conduction band position of brookite is higher than those of anatase and rutile, the three-phase mixed structure can further accelerate the migration of photogenerated electrons at the phase interfaces, which is beneficial to higher photocatalytic performance [10]. Kaplan et al. [17] prepared  $\text{TiO}_2$  with anatase, rutile and brookite polymorph phases by combining sol–gel process and hydrothermal treatment. It has been proved that  $\text{TiO}_2$  with triphasic structure exhibits better photocatalytic activity than anatase or rutile.

It is widely recognized that the specific surface area of photocatalysts is an important factor to photocatalytic performance. Many studies have been devoted to improving photocatalytic activity by increasing the specific surface area of  $\text{TiO}_2$ . The results of Aguilar et al.'s work reveal that the photocatalytic activity is enhanced owing to the increase of specific surface area after Cu doping [18]. It is reported by Zhang et al. [19] that the specific surface area of P25 increases from  $55.7 \text{ m}^2/\text{g}$  to  $78.7 \text{ m}^2/\text{g}$  after combining with graphene, consequently, the photocatalytic performance is extremely improved.

In the present study, pure and Cu-doped  $\text{TiO}_2$  nanocomposites with anatase/brookite/rutile triphasic structure were prepared by a facile hydrothermal method. The prepared samples were systematically characterized and their photocatalytic activity was assessed through the decomposition of RhB under xenon lamp irradiation.

## 2 Experimental

### 2.1 Synthesis of pure and Cu-doped $\text{TiO}_2$ nanomaterials

5 mL butyl titanate was dissolved into 10 mL ethanol to obtain solution A. 1 mL hydrochloric acid (37%), 1 mL polyethylene glycol (600) and proper amounts copper nitrate trihydrate (0.036 g, 0.072 g, 0.108 g and 0.144 g) were dissolved into 15 mL distilled water to acquire solution B. Solution B was added dropwise into solution A to form a sol.

The obtained sol mixture was transferred into a polytetrafluoroethylene-lined autoclave. The temperature and time of hydrothermal treatment were  $180^\circ\text{C}$  and 12 h. After the reactions, samples were washed and dried at  $100^\circ\text{C}$  and finally Cu-doped  $\text{TiO}_2$  nanocomposites were obtained. The Cu/Ti molar ratios are 1%, 2%, 3% and 4%. For simplicity,  $x\text{Cu-doped TiO}_2$  ( $x = 1\%, 2\%, 3\%$  and 4%) is labelled as  $x\text{Cu-TiO}_2$  ( $x = 1\%, 2\%, 3\%$  and 4%). Pure  $\text{TiO}_2$  nanocrystalline can be obtained without adding copper nitrate trihydrate in solution B.

### 2.2 Characterization

X-ray diffraction (XRD) patterns were recorded with a diffractometer (DX-2700, China). The test voltage is 40 kV, the test current is 30 mA, the scanning speed is  $0.06^\circ/\text{s}$ , and the scanning angle is  $20^\circ$ - $70^\circ$ . Raman spectra were measured using a Micro-Raman Renishaw spectrometer (Andor SR-500i, Britain)

equipped with an argon laser (532 nm). The surface morphologies were determined by a field-emission scanning electron microscope with a working voltage of 5 kV (SEM, FEI-Inspect F50, USA) and a transmission electron microscope with an acceleration voltage of 200 kV (TEM and HRTEM, FEI-Tecnai G2 F20, USA). X-ray photoelectron spectra (XPS) were recorded using a spectrometer using Mg ka at 12 kV and 12 mA (XSAM800, Britain). The optical properties were tested by UV-Vis diffuse reflectance spectra from 200–800 nm (DRS, UV-3600 spectrophotometer, Japan) and photoluminescence spectra (PL, F-4600 spectrophotometer with a 150 W xenon lamp (excitation wavelength 300 nm), Japan). A V-sorb 2800S surface area analyzer (China) was used to measure the BET specific surface area. The pore size distribution and pore volumes were obtained using the Barrett-Joyner-Halenda (BJH) method.

## 2.3 Photocatalytic test

The photocatalytic property of the obtained photocatalysts was evaluated through the degradation of RhB in aqueous solution. 100 mL RhB solution (10 mg/L) and 0.1 g photocatalyst powder were added into a beaker, and then stirred 30 min in dark. Afterwards, a 250 W xenon lamp with the emission wavelength from 300 nm to 800 nm was turned on as light source. The degradation of RhB was tested by measuring the absorbance at 553 nm every 10 min. The degradation degree ( $D$ ) was determined by the formula as follows:

$$D = (A_0 - A_t)/A_0 \text{, where } A_0 \text{ and } A_t \text{ are the initial absorbance and absorbance at time "t", respectively.}$$

## 3 Results And Discussion

### 3.1 XRD analysis

Figure 1 exhibits the XRD patterns of pure TiO<sub>2</sub> and Cu-TiO<sub>2</sub>. For both pure TiO<sub>2</sub> and Cu-TiO<sub>2</sub> samples, the diffraction peaks appear at  $2\theta = 25.3^\circ$ ,  $37.7^\circ$  and  $48.0^\circ$ , ascribing to the (101), (004) and (200) crystal planes of anatase structure (JCPDS 21-1272). Meanwhile, peaks at  $27.4^\circ$ ,  $36.1^\circ$  and  $54.3^\circ$  can be attributed to the (110), (101) and (211) planes of rutile TiO<sub>2</sub> (JCPDS 21-1276). Furthermore, the peaks appear at  $2\theta = 25.2^\circ$ ,  $25.4^\circ$  (overlapping with anatase (101) plane) and  $30.8^\circ$ , corresponding to the (120), (111) and (121) crystal planes of brookite TiO<sub>2</sub> (JCPDS 29-1360). The simultaneous appearance of the diffraction peaks corresponding to anatase, rutile and brookite structures indicates that the three phases coexist in both pure TiO<sub>2</sub> and Cu-TiO<sub>2</sub>. The mass fractions of anatase ( $W_a$ ), brookite ( $W_b$ ) and rutile ( $W_r$ ) can be calculated as follows:

$$W_a = K_a A_a / (K_a A_a + K_b A_b + K_r A_r)$$

$$W_b = K_b A_b / (K_a A_a + K_b A_b + K_r A_r)$$

$$W_r = K_r A_r / (K_a A_a + K_b A_b + K_r A_r)$$

where  $K_a$  (0.886) and  $K_b$  (2.721) are correction coefficients.  $A_a$ ,  $A_b$  and  $A_r$  express the peak intensities of anatase (101), brookite (121) and rutile (110) planes, respectively [20, 21]. The crystallite size was

calculated by Scherre's formula. For anatase, rutile and brookite,  $\beta$  are the half widths of the diffraction peaks of anatase (101), rutile (110), and brookite (121) planes, respectively [22, 23]. The phase composition and the average crystallite size of samples are summarized in Table 1. It can be seen that the content of anatase decreases and the content of rutile increases after Cu doping, which shows that the addition of Cu is conducive to the transformation from anatase to rutile. Since  $\text{Cu}^{2+}/\text{Cu}^+$  ion radius (0.073/0.077 nm) is close to  $\text{Ti}^{4+}$  ion radius (0.0605 nm),  $\text{Cu}^{2+}/\text{Cu}^+$  can enter into  $\text{TiO}_2$  lattice to replace  $\text{Ti}^{4+}$  ions and does not react with  $\text{TiO}_2$  to generate new crystal phase. This is in line with the earlier literatures [1, 13, 14]. When reaching a certain concentration, the Cu element is dispersed in the form of oxide on the surface of  $\text{TiO}_2$  particles. Therefore, the Cu-related diffraction peak cannot be detected in XRD patterns.

Table 1  
Phase composition and average crystallite size of pure  $\text{TiO}_2$  and  $\text{Cu}-\text{TiO}_2$ .

Photocatalysts	Phase composition (%) / Crystallite size (nm)		
	Anatase/Crystallite size	Rutile/Crystallite size	Brookite/Crystallite size
pure $\text{TiO}_2$	59.0% / 9.2	21.4% / 21.4	19.6% / 13.0
1% $\text{Cu}-\text{TiO}_2$	43.4% / 9.4	32.8% / 19.4	23.8% / 12.3
2% $\text{Cu}-\text{TiO}_2$	36.2% / 10.2	46.0% / 27.3	17.8% / 11.9
3% $\text{Cu}-\text{TiO}_2$	50.6% / 9.4	25.8% / 20.5	23.6% / 11.8
4% $\text{Cu}-\text{TiO}_2$	37.2% / 9.9	39.6% / 27.7	23.2% / 18.7

## 3.2 Raman analysis

To further confirm the crystal structure of the as-prepared samples, Raman measurement has been employed to distinguish the three structures of  $\text{TiO}_2$  and the results are shown in Fig. 2. The intense Raman bands located at  $398 \text{ cm}^{-1}$ ,  $517 \text{ cm}^{-1}$  and  $640 \text{ cm}^{-1}$  ascribe to anatase structure [14, 17]. The bands centered at  $244 \text{ cm}^{-1}$  and  $444 \text{ cm}^{-1}$  can be attributed to rutile structure, while the bands centered at  $320 \text{ cm}^{-1}$  and  $363 \text{ cm}^{-1}$  are for brookite structure [10, 16, 17]. The Raman spectra confirm that there are anatase/rutile/brookite three phases coexistence in pure  $\text{TiO}_2$  and  $\text{Cu}-\text{TiO}_2$ , which is in line with XRD results.

## 3.3 SEM and TEM analyses

Figure 3 depicts the SEM images of pure  $\text{TiO}_2$  (a) and 1% $\text{Cu}-\text{TiO}_2$  (b). It is observed that pure  $\text{TiO}_2$  consists of nanoparticles and a few nanorods. 1% $\text{Cu}-\text{TiO}_2$  is also made of nanoparticles and nanorods.

The TEM image of 1%Cu–TiO<sub>2</sub> is shown in Fig. 3c, which reveals that the particles size in 1%Cu–TiO<sub>2</sub> ranges from 10 to 20 nm. The nanorods in 1%Cu–TiO<sub>2</sub> have a length of 100 nm and a width of 10 nm approximately. Figure 3d presents the HRTEM image of 1%Cu–TiO<sub>2</sub>. The marked lattice distances are 0.353 nm, 0.250 nm and 0.293 nm, which can be attributed to the (101) crystal plane of anatase, the (101) crystal plane of rutile and the (121) crystal plane of brookite [24], respectively. Figure 3e-j present the STEM mapping of 1%Cu–TiO<sub>2</sub>. It can be seen that there are three elements (Ti, O, Cu) in the sample and are distributed in the matrix basically evenly.

### 3.4 XPS analysis

Figure 4 shows the XPS results of pure TiO<sub>2</sub> and 1%Cu–TiO<sub>2</sub>. Total spectra are displayed in Fig. 4a, from which the signals of Ti, O and C elements can be detected in pure TiO<sub>2</sub>. Meanwhile, a peak of Cu 2p appears in 1%Cu–TiO<sub>2</sub> spectrum, which confirms that Cu exists in TiO<sub>2</sub> via doping. Figure 4b shows the high-resolution spectra of Ti 2p. The spectrum of pure TiO<sub>2</sub> has two peaks at 464.2 eV and 458.4 eV corresponding to Ti 2p<sub>1/2</sub> and Ti 2p<sub>3/2</sub>, suggesting that the chemical state of Ti element is + 4 [2]. Similarly, two peaks at 463.8 eV and 458.1 eV in the spectrum of 1%Cu–TiO<sub>2</sub>, which means Ti ions exist as Ti<sup>4+</sup>. The high-resolution spectra of O 1s are shown in Fig. 4c. The peaks include lattice oxygen (O<sub>L</sub>) peak at 530.0 eV and surface hydroxyl groups (O<sub>H</sub>) peak at 532.2 eV in pure TiO<sub>2</sub> [1, 25, 26]. The peaks for O<sub>L</sub> and O<sub>H</sub> of 1%Cu–TiO<sub>2</sub> are situated at 529.5 eV and 532.0 eV, separately. In photodegradation process, ·OH radicals are formed as the results of the reaction between surface hydroxyl groups and photoinduced holes, which possess strong oxidation ability. Therefore, more surface hydroxyl groups are beneficial to photocatalytic activity [27, 28]. The ratio of surface hydroxyl groups can be calculated from the deconvolution area of the two peaks [28]. The integral areas of O<sup>2-</sup> (O<sub>L</sub>) and OH<sup>-</sup> (O<sub>H</sub>) peaks are 46638 and 7391 in pure TiO<sub>2</sub> and the proportion of O<sub>H</sub> is 7391 / (46638 + 7391) = 13.7%. The integral areas of O<sub>L</sub> and O<sub>H</sub> peaks are 45270 and 8666 in 1%Cu–TiO<sub>2</sub> and the proportion of O<sub>H</sub> is 8666 / (45270 + 8666) = 16.1%. The calculation results are convinced that the surface hydroxyl group ratio increases after Cu doping. Compared to the Ti 2p and O 1s peaks of pure TiO<sub>2</sub>, the peaks of 1%Cu–TiO<sub>2</sub> shift to lower binding energy, which proves the formation of Ti-O-Cu bonds [1, 25]. The shift to lower binding energy probably because there is a shift in electron density from a lower electronegative Ti (1.54, Pauling value) to a higher electronegative Cu (1.90, Pauling value) atom [8]. Figure 4d displays the high-resolution spectrum Cu 2p of 1%Cu–TiO<sub>2</sub>. It is observed that the peaks for Cu<sup>2+</sup> are located at 933.4 and 952.3 eV and the peak for Cu<sup>+</sup> is located at 957.8 eV. The peak at 943.7 eV is related to the shock peak of CuO [29, 30].

### 3.5 DRS analysis

The diffuse reflectance spectroscopy test was carried out to examine the optical property of obtained photocatalysts and the DRS spectra are exhibited in Fig. 5a. The Kubelka–Munk function for diffuse reflectance is  $F(R) = (1-R)^2/2R$  [18]. Because F(R) is proportionality to the absorption coefficient  $\alpha$ , it can be obtained according to the Tauc's formula [31–33]. The plots of  $(ahv)^{1/2}$  versus the photon energy ( $hv$ )

were demonstrated in Fig. 5b. The band gap energy values of pure  $\text{TiO}_2$ , 1%Cu– $\text{TiO}_2$ , 2%Cu– $\text{TiO}_2$ , 3%Cu– $\text{TiO}_2$  and 4%Cu– $\text{TiO}_2$  are 3.06 eV, 3.07 eV, 3.02 eV, 2.96 eV and 3.04 eV, separately. It is worth noting that the absorption of 2%Cu– $\text{TiO}_2$  and 3%Cu– $\text{TiO}_2$  in the ultraviolet region is lower than that of the pure sample, which hinders the absorption of the light source and is not conducive to photocatalytic activity.

### 3.6 PL analysis

Since photoluminescence emission is derived from the recombination of photoinduced holes and electrons, it can provide accurate data of the separation of photoinduced pairs [34–36]. The PL spectra of pure  $\text{TiO}_2$  and Cu– $\text{TiO}_2$  are shown in Fig. 6 and it is found that the addition of Cu does not bring new emission peak but only changed the peak intensity. The main peaks around 412 nm can be ascribed to the band gap transition [36, 37]. The peaks arranged from 450 nm to 470 nm are attributed to the transition of charge carriers [36, 38]. All the Cu– $\text{TiO}_2$  samples show lower peak intensity than pure  $\text{TiO}_2$ , which indicates that the recombination of photoinduced electrons and holes is hindered by Cu adding effectively. Remarkably, the PL intensity decreases with the increase of Cu concentration, implying that the higher doping amount is, the more favorable it is to suppress the recombination of photogenerated electrons and holes.

### 3.7 BET analysis

Figure 7 presents the  $\text{N}_2$  adsorption–desorption isotherms and the pore size distribution curves (inset of Fig. 7) of pure  $\text{TiO}_2$  and Cu– $\text{TiO}_2$ . All the photocatalysts exhibit the type IV isotherms with the H2 hysteresis loop in the range of high relative pressure, which are the characteristic of mesoporous materials (2–50 nm) [1, 10, 27, 37, 39]. The pore size distribution curves indicate that both pure  $\text{TiO}_2$  and Cu– $\text{TiO}_2$  have a narrow pore size distribution and the main pore diameters are ranged from 3 nm to 9 nm. The specific surface area, pore size and pore volume data are listed in Table 2. The specific surface area results reveal that Cu– $\text{TiO}_2$  samples show higher surface areas than pure  $\text{TiO}_2$ . Sibu et al. [40] and Adyani et al. [1] believe that the surface textural property is improved owing to the presence of Ti–O–M (M is the doping element) bonds, which may restrain the conformity and rearrangement of the primary crystals, leading to increase of surface area [26, 33].

Table 2  
Textural properties of pure TiO<sub>2</sub> and Cu–TiO<sub>2</sub>.

Photocatalysts	BET surface area (m <sup>2</sup> /g)	Pore volume	Average pore size (nm)
		(cm <sup>3</sup> /g)	
pure TiO <sub>2</sub>	140.8	0.286	6.9
1%Cu–TiO <sub>2</sub>	160.0	0.311	6.4
2%Cu–TiO <sub>2</sub>	195.0	0.307	5.9
3%Cu–TiO <sub>2</sub>	177.5	0.279	6.2
4%Cu–TiO <sub>2</sub>	211.1	0.334	6.1

### 3.8 Photocatalytic activity analysis

Figure 8a shows the degradation degree of RhB relative to pure TiO<sub>2</sub> and Cu–TiO<sub>2</sub> under xenon lamp irradiation for 30 min. RhB was not degraded under illumination without photocatalyst, implying that the degradation of RhB should be attributed to the photodegradation of photocatalysts. The degradation degrees of pure TiO<sub>2</sub>, 1%Cu–TiO<sub>2</sub>, 2%Cu–TiO<sub>2</sub>, 3%Cu–TiO<sub>2</sub> and 4%Cu–TiO<sub>2</sub> are 90.0%, 93.5%, 91.8%, 86.2% and 92.5%, respectively. It is clear that all the photocatalysts show considerable photocatalytic activity, which attributes to relatively high specific surface areas (> 140 m<sup>2</sup>/g) and the anatase/rutile/brookite triphasic structure.

1%Cu–TiO<sub>2</sub> shows higher photocatalytic efficiency than pure TiO<sub>2</sub> because of its less recombination rate and higher surface area compared to pure TiO<sub>2</sub>. However, as the amount of doping content increases, the degradation degrees slightly decrease in 2%Cu–TiO<sub>2</sub> and 3%Cu–TiO<sub>2</sub> samples. The effect of doping amount on suppressing the recombination of photoinduced pairs is controversial. Several studies show that there is an optimal concentration in doping, and the inhibition of photogenerated electrons and holes is weakened when the concentration exceeds the optimal value [41–43]. The authors believe that excessive doping content will generate new recombination centers, which is not conducive to the migration of photogenerated electrons and holes. Correspondingly, it has also been documented that the higher the doping amount, the higher inhibition effect [44–46]. The inconsistent results may be caused by different preparation methods and processes. In the present study, when the concentration of Cu/Ti reaches 4%, it is still conducive to the separation of photogenerated electrons and holes. Therefore, the decreased photocatalytic activity of 2%Cu–TiO<sub>2</sub> and 3%Cu–TiO<sub>2</sub> should not be ascribed to the enhancement of recombination rate. On the other hand, DRS results shows that the absorption of 2%Cu–TiO<sub>2</sub> and 3%Cu–TiO<sub>2</sub> in the ultraviolet region is lower than that of the pure sample, which may be attributed to the fact that the excessive Cu doping content produce more CuO and Cu<sub>2</sub>O clusters on TiO<sub>2</sub> surface, decreasing the light utilization and photocatalytic efficiency [44]. However, if the specific surface

area further increases, the disadvantage caused by CuO and Cu<sub>2</sub>O covering TiO<sub>2</sub> surface can be offset. Therefore, the photocatalytic efficiency of 4%Cu–TiO<sub>2</sub> increases slightly since it possesses the highest specific surface area (211.1 m<sup>2</sup>/g).

Figure 8b displays the kinetics fitting curves of  $\ln(C/C_0) = -k t$  of the photocatalysts [47]. The apparent first-order rate constants  $k$  of pure TiO<sub>2</sub>, 1%Cu–TiO<sub>2</sub>, 2%Cu–TiO<sub>2</sub>, 3%Cu–TiO<sub>2</sub> and 4%Cu–TiO<sub>2</sub> are 0.071 min<sup>-1</sup> ( $R^2 = 0.948$ ), 0.091 min<sup>-1</sup> ( $R^2 = 0.977$ ), 0.083 min<sup>-1</sup> ( $R^2 = 0.971$ ), 0.063 min<sup>-1</sup> ( $R^2 = 0.948$ ) and 0.084 min<sup>-1</sup> ( $R^2 = 0.992$ ), respectively.

### 3.9 The degradation mechanism

·O<sub>2</sub><sup>-</sup> radicals react with nitro-blue tetrazolium (NBT) to form purple precipitates, therefore, the lower NBT absorbance indicates more ·O<sub>2</sub><sup>-</sup> radicals generated. 2, 3-HBA is obtained by the reaction of salicylic acid (SA) with ·OH radicals, which has a special absorption at 510 nm. Therefore, the higher absorbance is, the higher the concentration of 2, 3-HBA is, indicating that more ·OH radicals are produced [48, 49]. Taking 1%Cu–TiO<sub>2</sub> as an example, the experiments are carried out. Figure 9a shows that the NBT absorbance decreases with increased illumination time, indicating that more and more purple precipitates are generated from the reaction between ·O<sub>2</sub><sup>-</sup> and NBT after illumination, which results in the consumption of NBT. The decreasing NBT absorbance indicates that the photogenerated electrons are excited to the conduction band after illumination and react with O<sub>2</sub> to form ·O<sub>2</sub><sup>-</sup> radicals. Figure 9b shows that 2, 3-HBA absorbance increases with the increased illumination time. Because 2, 3-HBA is obtained from the reaction between SA and ·OH, the increasing 2, 3-HBA absorbance indicates that ·OH radicals are formed under illumination.

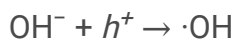
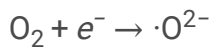
NBT and SA experiments confirm that ·O<sub>2</sub><sup>-</sup> and ·OH radicals are generated under illumination. Since ·O<sub>2</sub><sup>-</sup> radicals come from the reaction of photogenerated electrons with O<sub>2</sub>, and ·OH radicals originate from the reaction of photogenerated hole with OH<sup>-</sup>, the numbers of ·O<sub>2</sub><sup>-</sup> and ·OH radicals can be used to measure the separation of photogenerated charge under the same conditions. Figure 10a shows that the NBT absorbance of pure TiO<sub>2</sub> is higher than that of 1%Cu–TiO<sub>2</sub>, which suggests that 1%Cu–TiO<sub>2</sub> generates more ·O<sub>2</sub><sup>-</sup> radicals than pure TiO<sub>2</sub>. Figure 10b shows that the 2, 3-HBA absorbance of pure TiO<sub>2</sub> is lower than that of 1%Cu–TiO<sub>2</sub>, indicating that 1%Cu–TiO<sub>2</sub> produces more ·OH radicals. Therefore, 1%Cu–TiO<sub>2</sub> shows the higher separation rate of photogenerated charges than pure TiO<sub>2</sub>. Cu doping enhances the quantum efficiency, which is consistent with the PL spectra.

In order to compare the photogenerated charge separation of triphasic photocatalysts and the monophasic/biphasic photocatalysts, the NBT and 2, 3-HBA absorbances of 1%Cu–TiO<sub>2</sub> were measured and the results are shown in Fig. 11. Compared to monophasic/biphasic 1%Cu–TiO<sub>2</sub>, triphasic 1%Cu–TiO<sub>2</sub> has lower NBT absorbance and higher 2, 3-HBA absorbance, which indicates that triphasic 1%Cu–

$\text{TiO}_2$  produces more photogenerated charges and has the highest quantum efficiency. Accordingly, the photocatalytic activity of triphasic 1%Cu– $\text{TiO}_2$  is higher than that of monophasic/biphasic 1%Cu– $\text{TiO}_2$ .

To determine the active species in the process of photodegradation, isopropanol (IPA), benzoquinone (BQ) and ammonium oxalate (AO) were added to capture  $\cdot\text{OH}$ ,  $\cdot\text{O}_2^-$  and  $\text{h}^+$ , respectively. The degradation results of 1%Cu– $\text{TiO}_2$  in the presence of different scavengers are shown in Fig. 12. When BQ, AO and IPA were added, the degradation rate of 1%Cu– $\text{TiO}_2$  decreases from 93.5–36.0%, 68.2% and 91.4%, respectively. Obviously, the degradation rate is significantly decreased with BQ adding. The degradation rate decreases slightly in the presence of AO and IPA. Since BQ captures  $\cdot\text{O}_2^-$ , AO captures  $\text{h}^+$ , and IPA captures  $\cdot\text{OH}$ , therefore,  $\text{O}_2^-$  radical is the main active specie, and  $\text{h}^+$  and  $\cdot\text{OH}$  are subsidiary in the degradation process.

Based on the above experimental results, the photocatalytic degradation mechanism of 1%Cu– $\text{TiO}_2$  versus RhB is proposed in Fig. 13. When  $\text{TiO}_2$  is exposed to light source, electrons in valence band (VB) are excited to conduction band (CB), producing corresponding holes in VB. The photoinduced electrons in anatase and brookite will transfer to rutile, which accelerates the movement of photoinduced electrons, prolongs the lifetime and inhibits the recombination of photoinduced pairs effectively [10, 17]. Moreover, the conversion of Cu ions and the photocatalytic process of 1%Cu– $\text{TiO}_2$  are as follows [44, 50]:



Consequently, the process of transformation between  $\text{Cu}^{2+}$  and  $\text{Cu}^+$  suppresses the recombination of photoinduced pairs, which is in favor of photocatalytic activity. The formed  $\cdot\text{O}_2^-$ ,  $\cdot\text{OH}$  radicals and  $\text{h}^+$  species have strong oxidizing properties and are able to degrade RhB into small inorganic molecules.

## 4 Conclusions

In this work, pure  $\text{TiO}_2$  and Cu– $\text{TiO}_2$  were synthesized by a hydrothermal process. XRD, Raman and HRTEM results confirm that the anatase/rutile/brookite triphasic structure form in both pure  $\text{TiO}_2$  and Cu– $\text{TiO}_2$  samples. SEM and TEM images show the particle sizes in the range of 10–20 nm. XPS results confirm that the Ti element exist in the form of  $\text{Ti}^{4+}$  and Cu is present in the  $\text{Cu}^{2+}$  and  $\text{Cu}^+$  oxidation states. Cu doping is beneficial to increase the surface hydroxyl group content of  $\text{TiO}_2$ . PL spectra show that the recombination of photogenerated electrons and holes is inhibited effectively with Cu addition and the inhibition enhances with the increase of Cu doping concentration. Pure  $\text{TiO}_2$  exhibits relatively

high BET specific surface area ( $140.8\text{ m}^2/\text{g}$ ) and Cu adding can further improve the specific surface area. The pore size distribution curves confirm that the obtained samples are mesoporous materials. RhB solution was employed as the target pollutant and the photocatalytic activity was tested under xenon lamp irradiation.  $\cdot\text{O}_2^-$  radicals play a major role in the photodegradation process. Triphasic 1%Cu–TiO<sub>2</sub> shows better photocatalytic property than monophasic/biphasic 1%Cu–TiO<sub>2</sub>. The degradation degree of 1%Cu–TiO<sub>2</sub> is 93.5% in 30 min, and the apparent first-order rate constant of 1%Cu–TiO<sub>2</sub> is  $0.091\text{ min}^{-1}$ , suggesting that it is a promising photocatalyst for dye wastewater treatment.

## Declarations

## Acknowledgements

This project was funded by the Applied Basic Research Programs of Sichuan Province (Grant Nos. 2019YJ0664, 2018JY0062), the Chengdu Technology Innovation Research and Development Project of Chengdu City (Grant No. 2019-YFYF-00013-SN) and the Training Program for Innovation of Sichuan Province (S202011079053, CDU-CX-2021527).

## References

1. S.M. Adyani, M. Ghorbani, *J. rare Earth.* **36**, 72–85 (2018)
2. N. Wei, H.Z. Cui, Q. Song, L.Q. Zhang, X.J. Song, K. Wang, Y.F. Zhang, J. Li, J. Wen, J. Tian, *Appl. Catal. B-environ.* **198**, 83–90 (2016)
3. X.D. Zhu, L.X. Pei, R.R. Zhu, Y. Jiao, R.Y. Tang, W. Feng, *Sci. Rep.* **8**, 14249–14257 (2018)
4. D.V. Dao, M.V.D. Bremt, Z. Koeller, T.K. Le, *Powder Technol.* **288**, 366–370 (2016)
5. T.H. Le, A.T. Bui, T.K. Le, *Powder Technol.* **268**, 173–176 (2014)
6. D. Yang, Y.Y. Sun, Z.W. Tong, Y.H. Nan, Z.Y. Jiang, *J. Hazard. Mater.* **312**, 45–54 (2016)
7. A.M. Abdulkarem, E.M. Elssfah, N.N. Yan, G. Demissie, Y. Yu, *J. Phys. Chem. Solids* **74**, 647–652 (2013)
8. V.B.R. Boppana, R.F. Lobo, *J. Catal.* **281.1**, 156–168 (2011)
9. F.C. Correia, M. Calheiros, J. Marques, J.M. Ribeiro, C.J. Tavares, *Ceram. Int.* **44**, 22638–22644 (2018)
10. H.L. Wang, X.Y. Gao, G.R. Duan, X.J. Yang, X.H. Liu, *J. Environ. Chem. Eng.* **3**, 603–608 (2015)
11. Y.F. Zhang, F. Fu, Y.Z. Li, D.S. Zhang, Y.Y. Chen, *Nanomaterials* **8**, 1032 (2018)
12. Z.L. Yang, J. Lu, W.C. Ye, C.S. Yu, Y.L. Chang, *Appl. Surf. Sci.* **392**, 472–480 (2017)
13. M.R.D. Khaki, M.S. Shafeeyan, A.A.A. Raman, W.M.A.W. Daud, *J. Mol. Liq.* **258**, 354–365 (2018)
14. M.C. Wu, P.Y. Wu, T.H. Lin, T.F. Lin, *Appl. Surf. Sci.* **430**, 390–398 (2018)
15. H. Li, X.J. Shen, Y.D. Liu, L.Z. Wang, J.Y. Lei, J.L. Zhang, *J. Alloy. Compd.* **646**, 380–386 (2015)
16. Y.F. Cao, X.T. Li, Z.F. Bian, A. Fuhr, D.Q. Zhang, J. Zhu, *Appl. Catal. B-Environ.* **180**, 551–558 (2016)

17. R. Kaplan, B. Erjavec, G. Dražić, J. Grdadolnikc, A. Pintar, *Appl. Catal. B—Environ.* **181**, 465–474 (2016)
18. T. Aguilar, J. Navas, R. Alcántara, C. Fernández-Lorenzo, J.J. Gallardo, G. Blanco, J. Martín-Calleja, *Chem. Phys. Lett.* **571**, 49–53 (2013)
19. Y.P. Zhang, C.X. Pan, *J. Mater. Sci.* **46**, 2622–2626 (2011)
20. L.K. Preethi, T. Mathews, M. Nand, S.N. Jha, C.S. Gopinath, S. Dash, *Appl. Catal. B—Environ.* **218**, 9–19 (2017)
21. H.Z. Zhang, J.F. Banfield, *J. Phys. Chem. B* **104**, 3481–3487 (2000)
22. V. Uvarov, I. Popov, *Mater. Charact.* **58**, 883–891 (2007)
23. B.K. Mutuma, G.N. Shao, W.D. Kim, H.T. Kim, *J. Colloid. Interf. Sci.* **442**, 1–7 (2015)
24. P.M. Dong, X.D. Cheng, Z.F. Huang, Y. Chen, Y.Z. Zhang, X.X. Nie, X.W. Zhang, *Mater. Rsc. Bull.* **97**, 89–95 (2018)
25. X.J. Yang, S. Wang, H.M. Sun, X.B. Wang, J.S. Lian, *T. Nonferr. Metal. Soc.* **25**, 504–509 (2015)
26. J.L. Li, X.T. Xu, X.J. Liu, C.Y. Yu, D. Yan, Z. Sun, L.K. Pan, *J. Alloy. Compd.* **679**, 454–462 (2016)
27. O. Avilés-García, J. Espino-Valencia, R. Romero, J.L. Rico-Cerda, M. Arroyo-Albiter, R. Natividad, *Fuel.* **198**, 31–41 (2017)
28. Z.M. Wang, B. Liu, Z.X. Xie, Y.M. Li, Z.Y. Shen, *Ceram. Int.* **42**, 13664–13669 (2016)
29. G. Córdoba, M. Viniegra, J.L.G. Fierro, J. Padilla, R. Arroyo, *J. Solid State Chem.* **138**, 1–6 (1998)
30. R. Bashiri, N.M. Mohamed, C.F. Kait, S. Sufian, M. Khatani, *J. Environ. Chem. Eng.* **5**, 3207–3214 (2017)
31. M. Shaban, A.M. Ashraf, M.R. Abukhadra, *Sci. Rep.* **8**, 781 (2018)
32. J. Tauc, R. Grigorovici, A. Vancu, *Phys. Status Solidi B* **15**, 627–637 (1966)
33. P. Makal, D. Das, *Appl. Surf. Sci.* **455**, 1106–1115 (2018)
34. Y.Z. Wang, Y.S. Wu, H. Yang, X.X. Xue, Z.H. Liu, *Vacuum.* **131**, 58–64 (2016)
35. J. Singh, A.K. Manna, R.K. Soni, *J. Mater. Sci—Mater. El.* **30**, 16478–16493 (2019)
36. X. Fan, J. Wan, E.Z. Liu, L. Sun, Y. Hu, H. Li, X.Y. Hu, J. Fan, *Ceram. Int.* **41**, 5107–5116 (2015)
37. X.F. Lei, X.X. Xue, H. Yang, *Appl. Surf. Sci.* **321**, 396–403 (2014)
38. B. Appavu, S. Thiripuranthagan, *Visible active N. J. Photoch. Photobio. A* **340**, 146–156 (2017)
39. B.K. Kaleji, S. Mirzaee, S. Ghahramani, S. Rezaie, N. Hosseinabadi, A. Fujishima, *J. Mater. Sci—Mater. El.* **29**, 12351–12359 (2018)
40. C.P. Sibu, S.R. Kumar, P. Mukundan, K.G.K. Warrier, *Chem. Mater.* **14**, 2876–2881 (2002)
41. T. Ali, A. Ahmed, U. Alam, I. Uddin, P. Tripathi, M. Muneer, *Mater. Chem. Phys.* **212**, 325–335 (2018)
42. S. Sood, A. Umar, S.K. Mehta, S.K. Kansal, *J. Colloid Interf. Sci.* **450**, 213–223 (2015)
43. X.X. Lin, F. Rong, D.G. Fu, C.W. Yuan, *Powder Technol.* **219**, 173–178 (2012)

44. V. Krishnakumar, S. Boobas, J. Jayaprakash, M. Rajaboopathi, B. Han, M. Louhi-Kultanen, *J. Mater. Sci–Mater. El.* **27**, 7438–7447 (2016)
45. X.D. Zhu, R.R. Zhu, L.X. Pei, H. Liu, L. Xu, J. Wang, W. Feng, Y. Jiao, W.M. Zhang, *J. Mater. Sci–Mater. El.* **30**, 21210–21218 (2019)
46. Z.H. Fan, F.M. Meng, J.F. Gong, H.J. Li, Z.L. Ding, B. Ding, *J. Mater. Sci–Mater. El.* **27**, 11866–11872 (2016)
47. Y. Zhang, T. Wang, M. Zhou, Y. Wang, Z.M. Zhang, *Ceram. Int.* **43**, 3118–3126 (2017)
48. J. Li, Y.J. Wan, Y.J. Li, G. Yao, B. Lai, *Appl. Catal. B–Environ.* **256**, 117782 (2019)
49. J.X. Qin, J. Wang, J.J. Yang, Y. Hu, M.L. Fu, D.Q. Ye, *Appl. Catal. B–Environ.* **267**, 118667 (2020)
50. H.W.P. Carvalho, M.V.J. Rocha, P. Hammer, T.C. Ramalho, *J. Mater. Sci.* **48**, 3904–3912 (2013)

## Figures

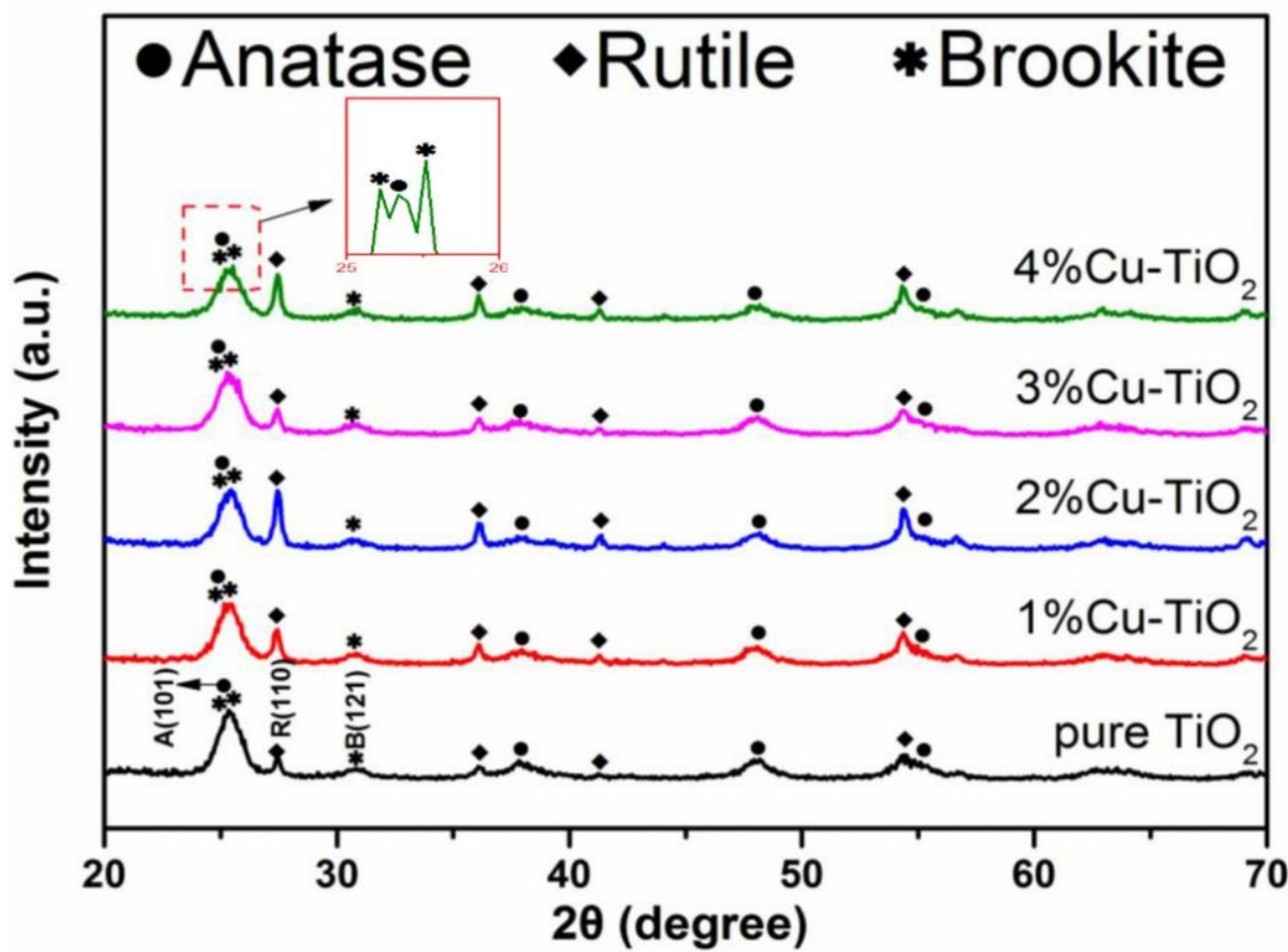


**Figure 1**

XRD patterns of pure TiO<sub>2</sub> and Cu-TiO<sub>2</sub>.

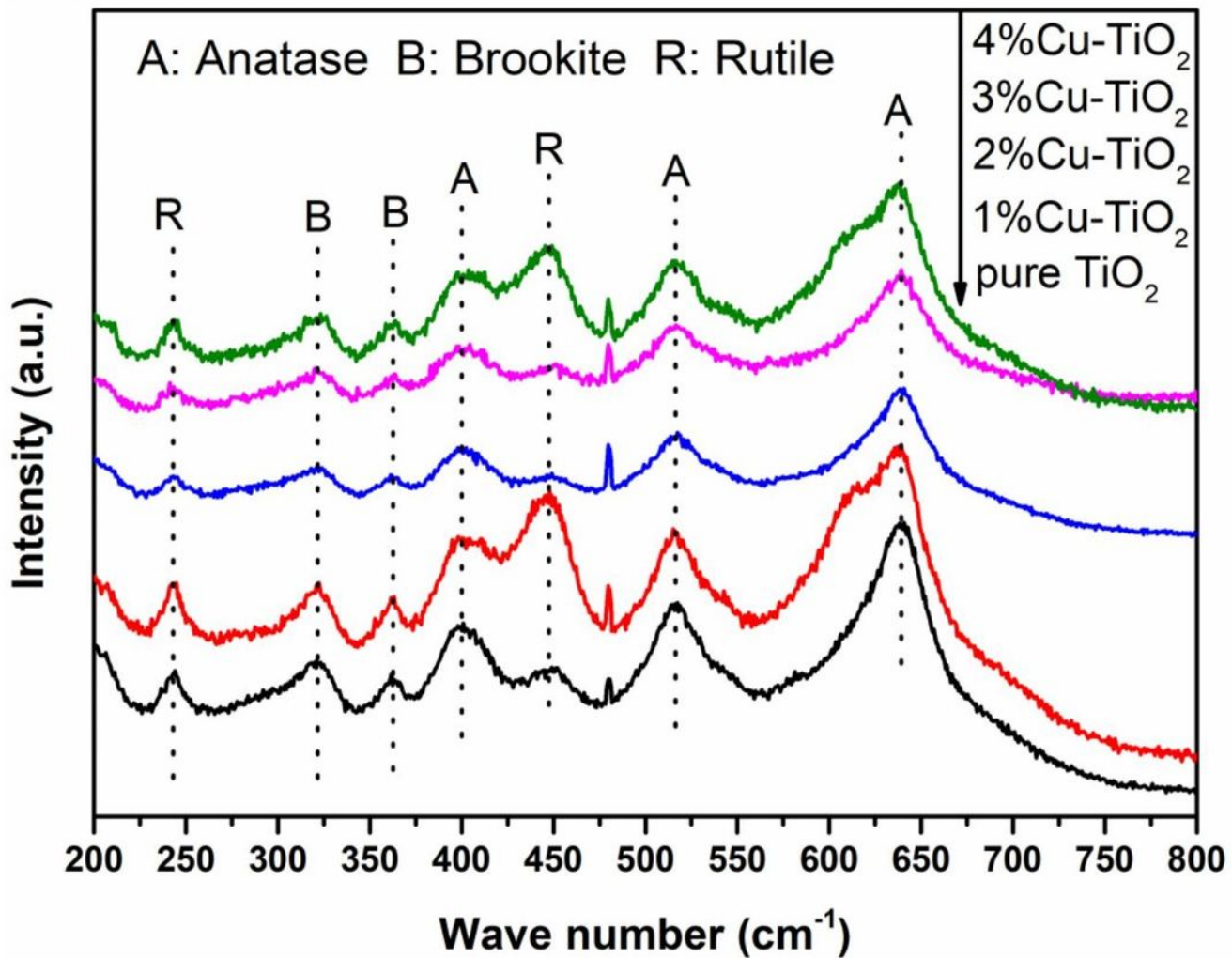
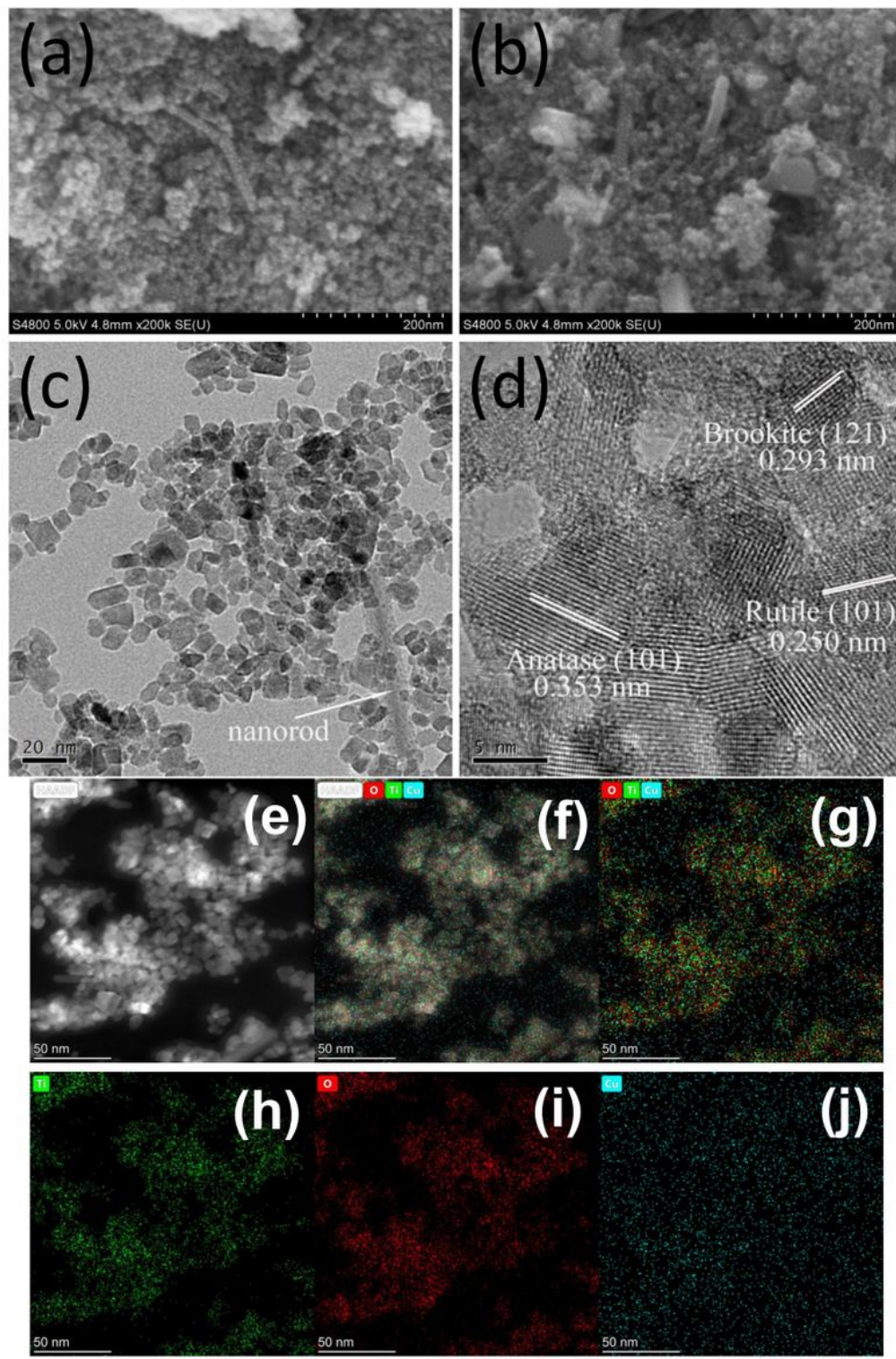


Figure 2

Raman spectra of pure TiO<sub>2</sub> and Cu-TiO<sub>2</sub>.



**Figure 3**

(a) SEM images of pure  $\text{TiO}_2$ , (b) SEM images of 1%Cu– $\text{TiO}_2$ , (c) TEM image of 1%Cu– $\text{TiO}_2$ , (d) HRTEM image of 1%Cu– $\text{TiO}_2$  and (f-j) STEM mapping of 1%Cu– $\text{TiO}_2$

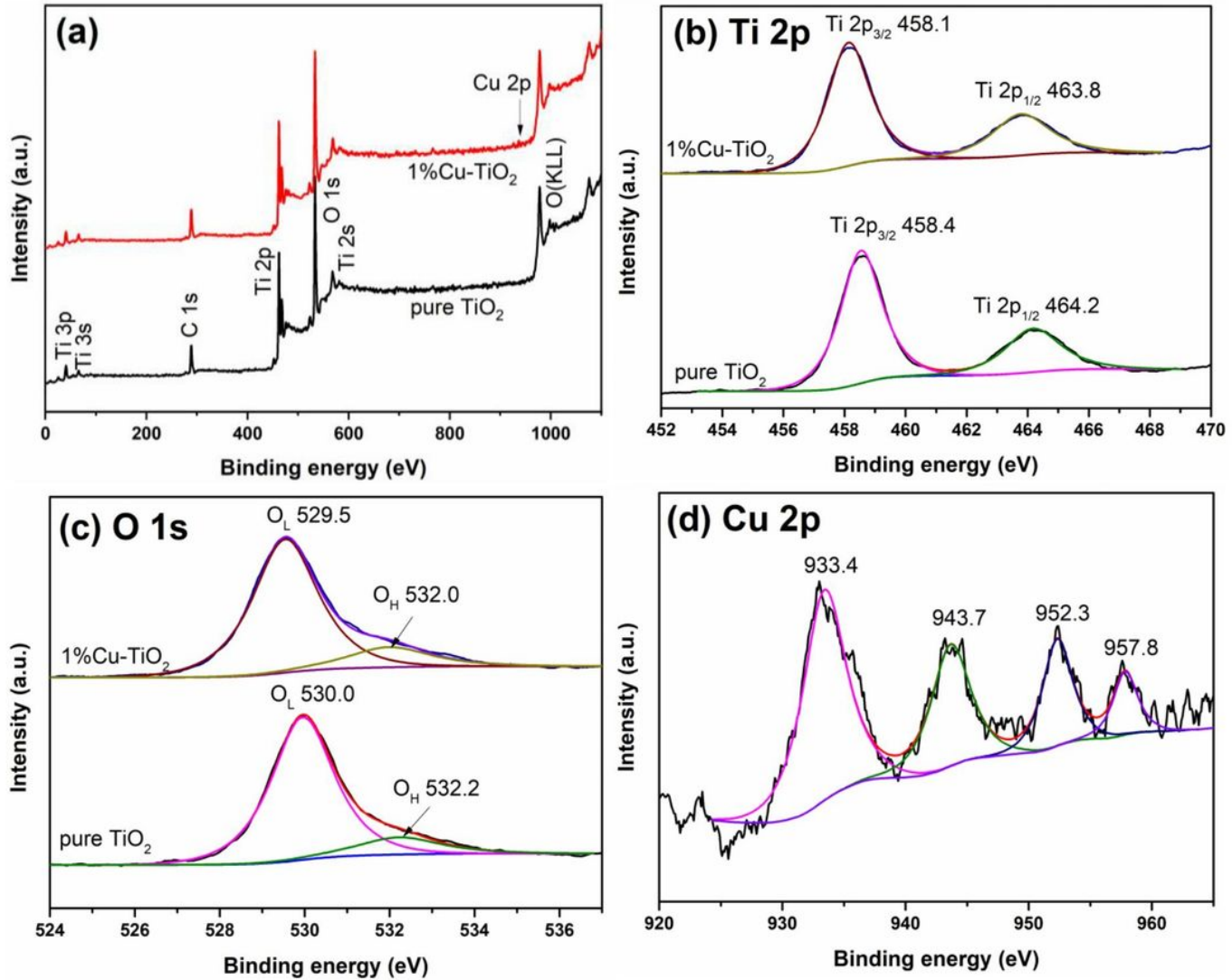


**Figure 4**

XPS spectra of pure TiO<sub>2</sub> and 1%Cu-TiO<sub>2</sub>.

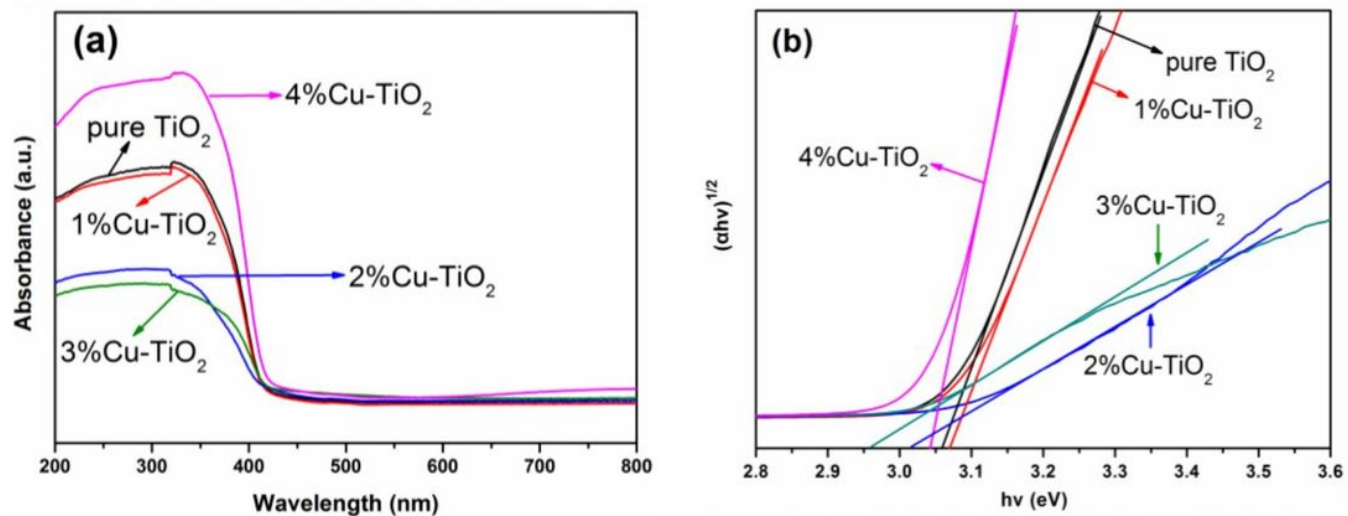


**Figure 5**

(a) Diffuse reflection spectra of pure TiO<sub>2</sub> and Cu-TiO<sub>2</sub>, (b) plots of  $(\alpha h\nu)^{1/2}$  versus the photon energy ( $h\nu$ ).

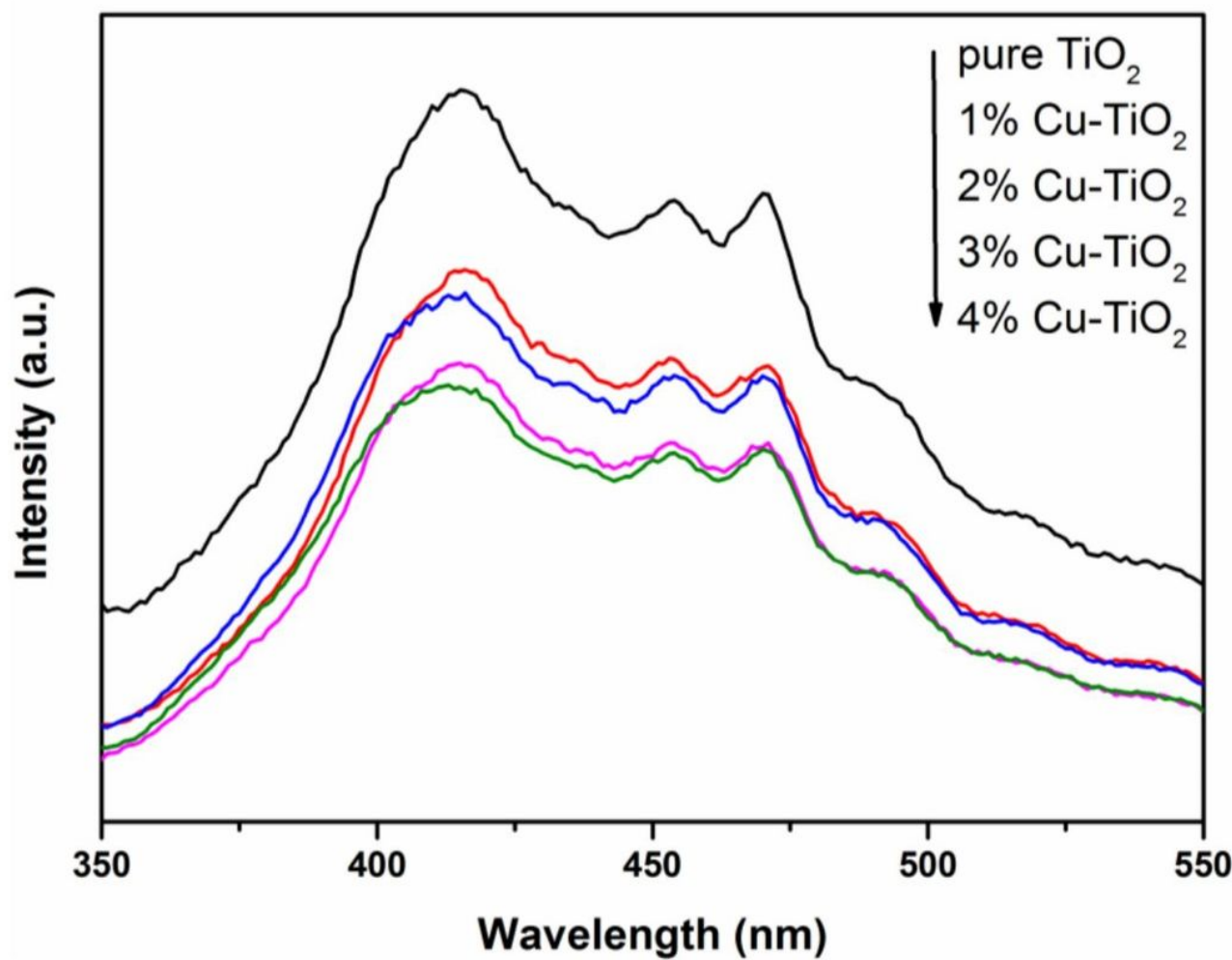


**Figure 6**

Photoluminescence (PL) spectra of pure  $\text{TiO}_2$  and  $\text{Cu}-\text{TiO}_2$ .

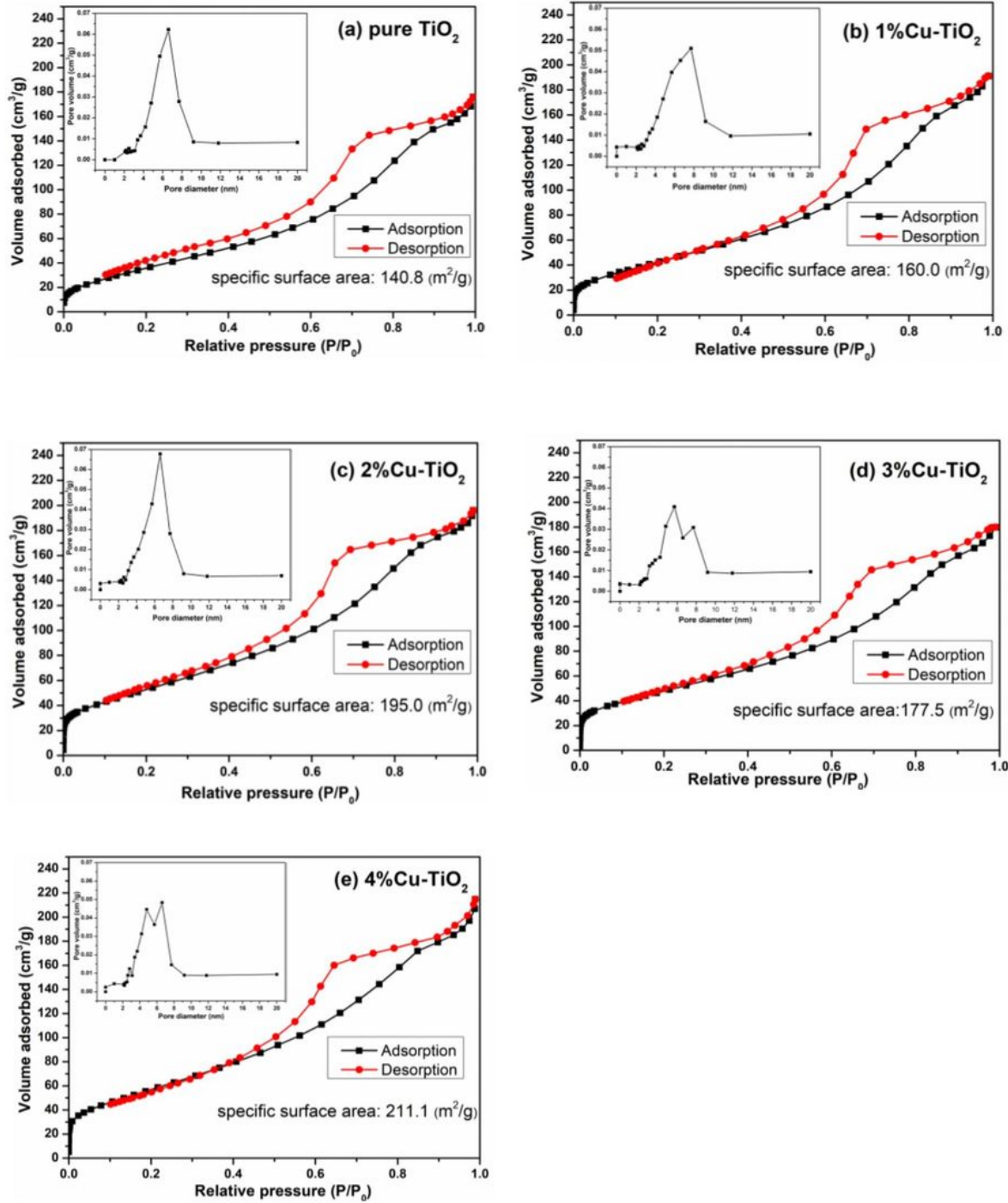


**Figure 7**

Nitrogen adsorption–desorption isotherms and pore size distribution curves of (a) pure  $\text{TiO}_2$ , (b) 1%Cu- $\text{TiO}_2$ , (c) 2%Cu- $\text{TiO}_2$ , (d) 3%Cu- $\text{TiO}_2$  and (e) 4%Cu- $\text{TiO}_2$

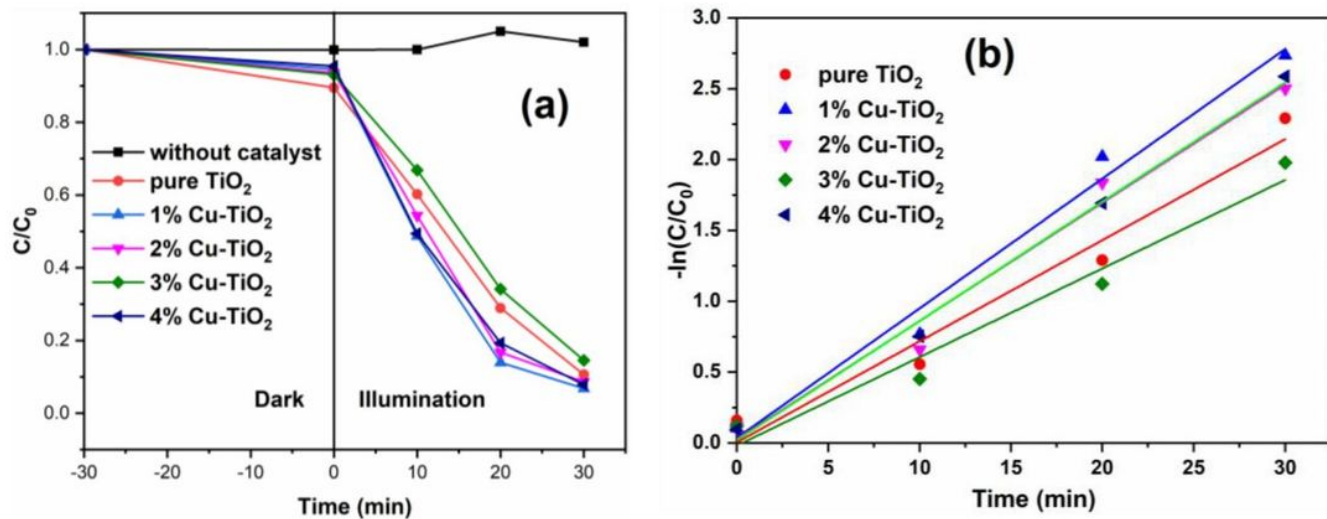


**Figure 8**

(a) Photocatalytic degradation of RhB for pure  $\text{TiO}_2$  and Cu-TiO<sub>2</sub>, (b) degradation kinetics curves of photocatalysts on RhB.

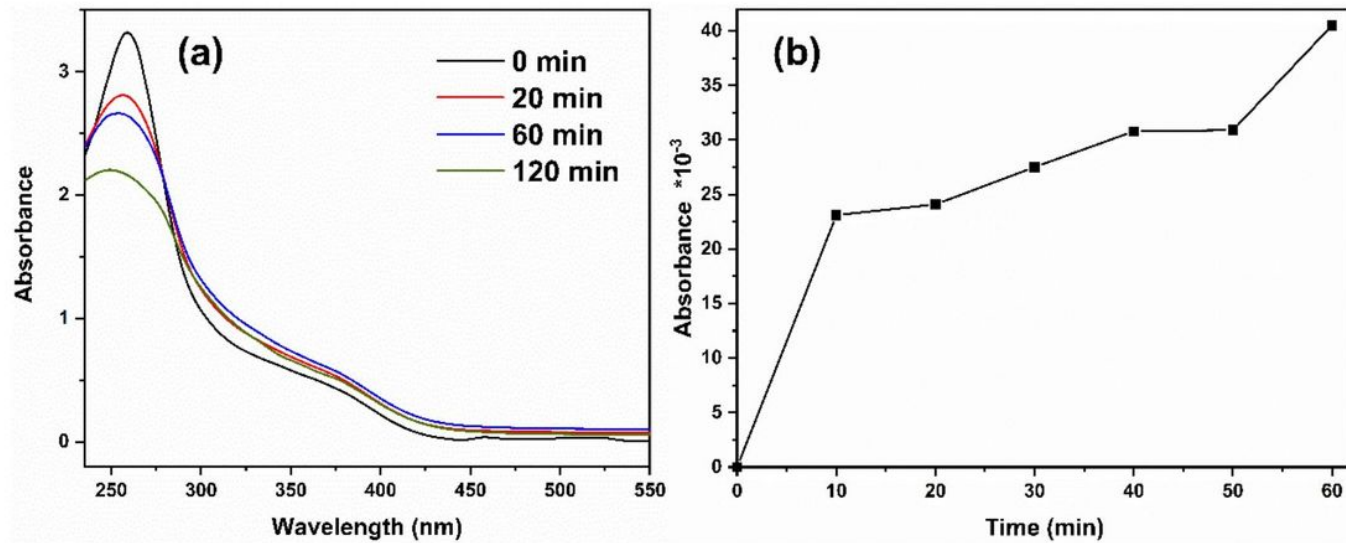


**Figure 9**

The absorbance curves of NBT (a) and 2,3-HBA (b) of 1%Cu-TiO<sub>2</sub>

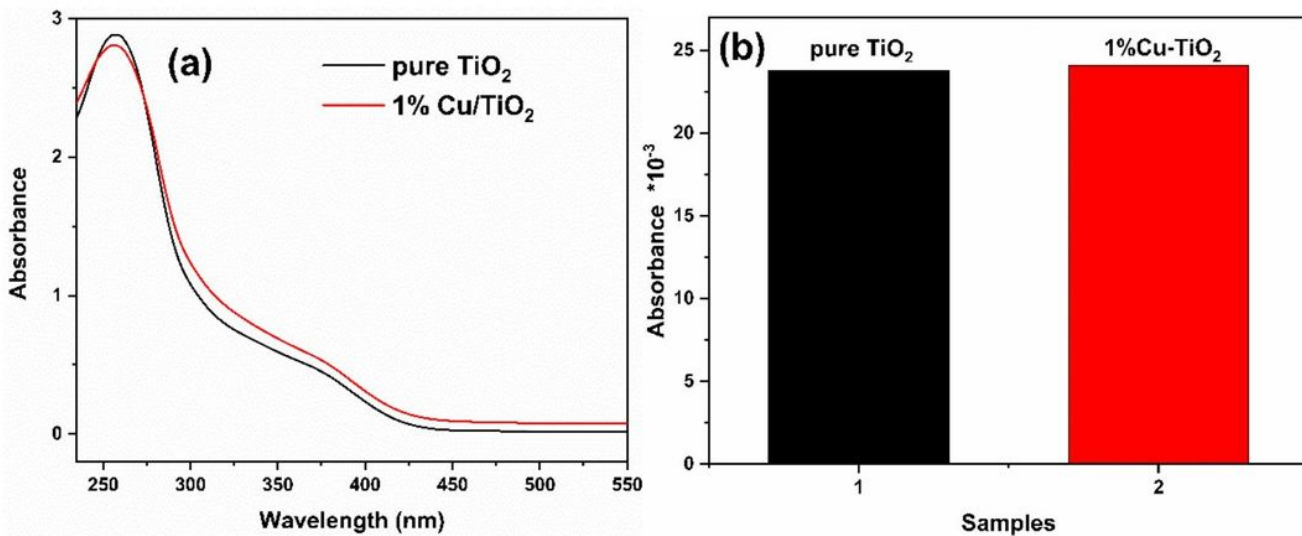
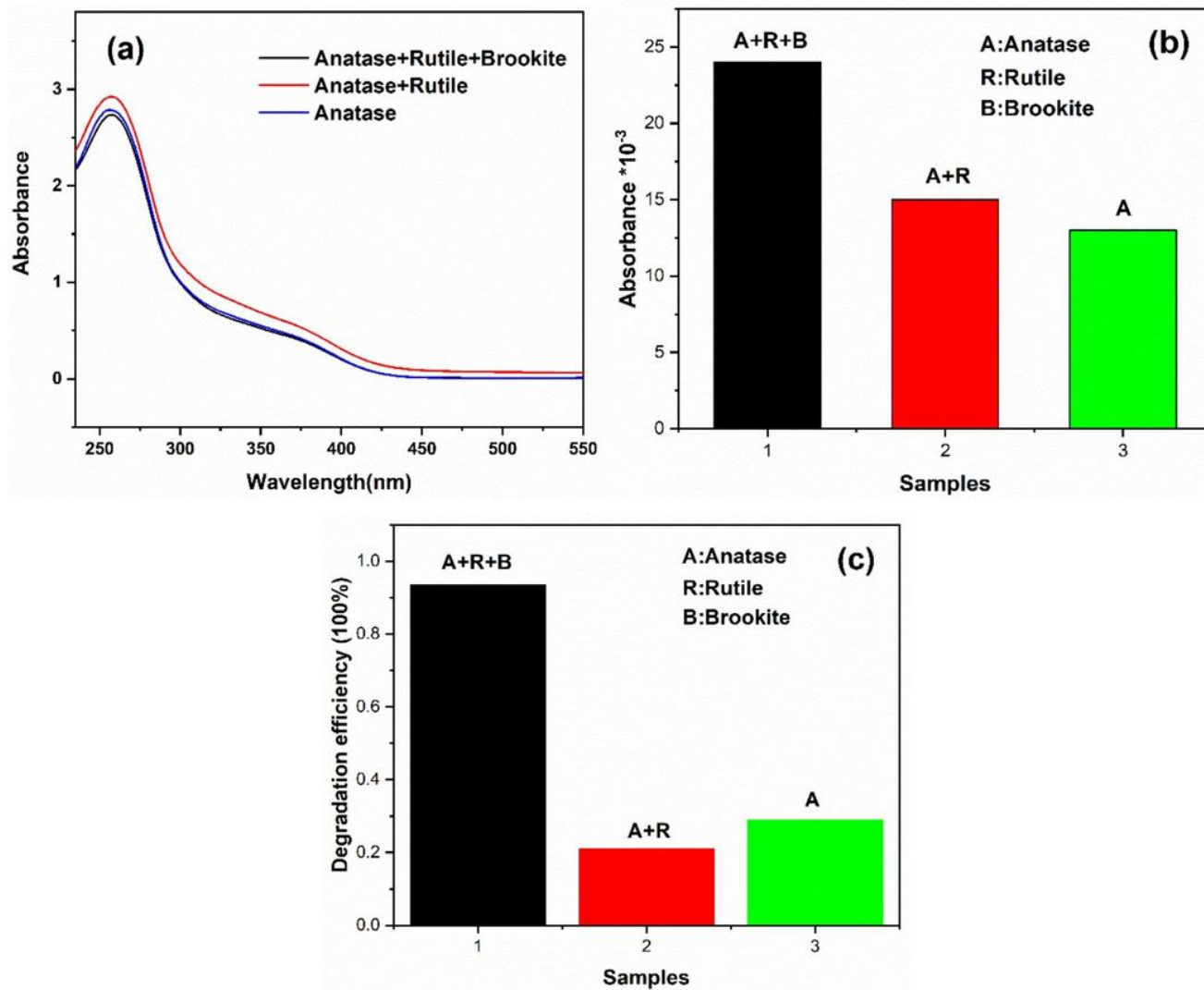


Figure 10

NBT (a) and 2, 3-HBA (b) absorbances of 1%Cu-TiO<sub>2</sub> and pure TiO<sub>2</sub>



**Figure 11**

NBT (a) and 2, 3-HBA (b) absorbances and degradation efficiency (c) of 1%Cu-TiO<sub>2</sub> with different phase structure

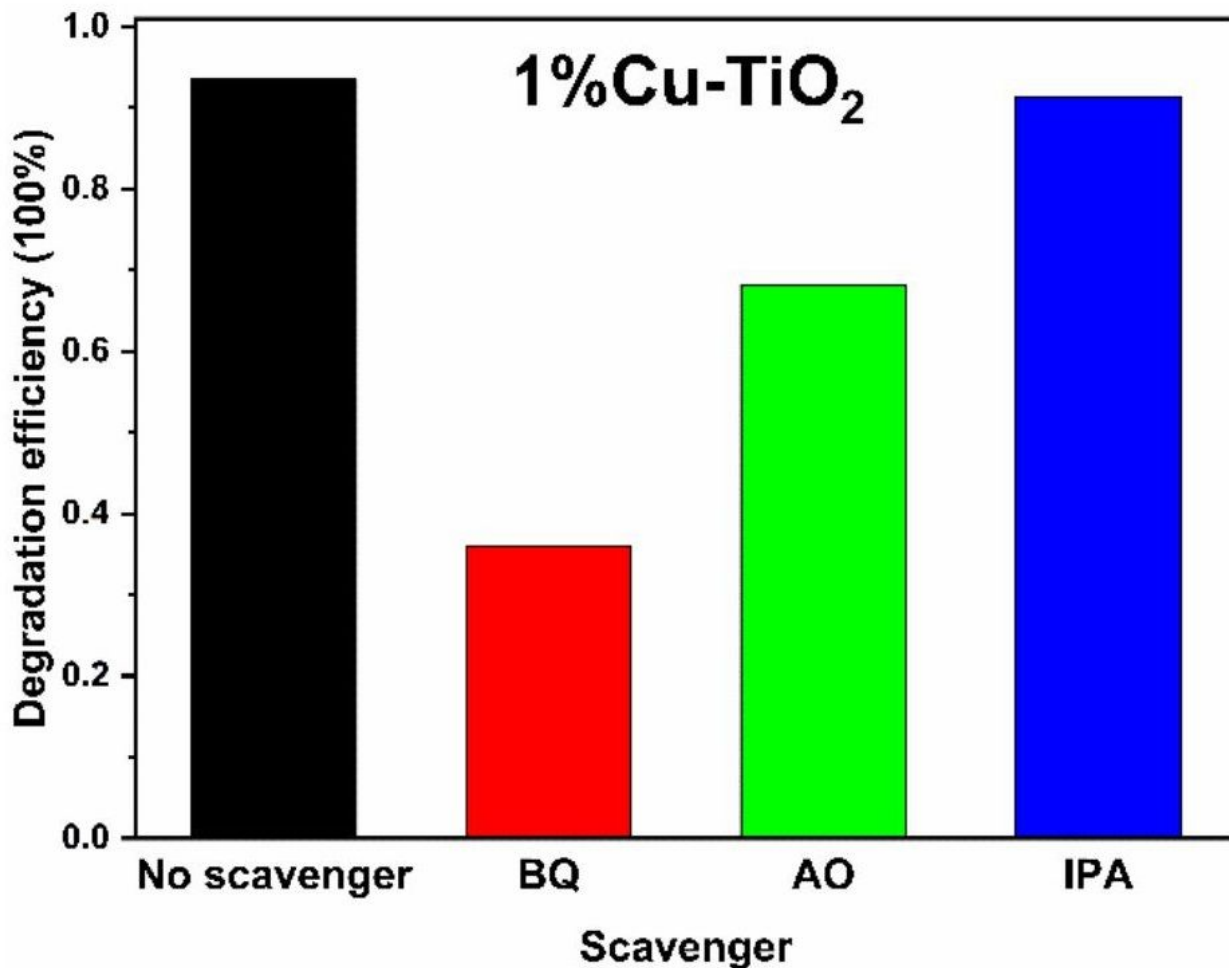


**Figure 12**

The degradation rate of 1%Cu-TiO<sub>2</sub> in the presence of different scavengers

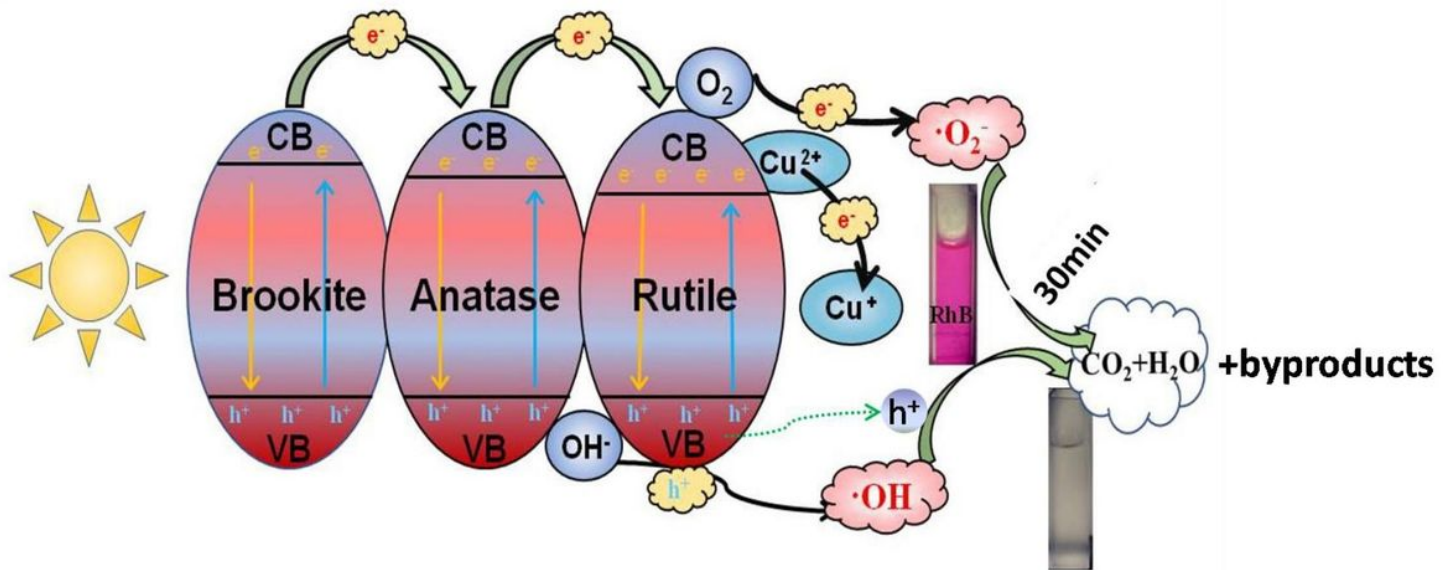


Figure 13

Schematic diagram of charge transfer and photodegradation of RhB for 1%Cu-TiO<sub>2</sub>